

# Where to Touch, How to Contact: Hierarchical RL-MPC Framework for Geometry-Aware Long-Horizon Dexterous Manipulation

Zhixian Xie

Arizona State University

Yu Xiang

UT Dallas

Michael Posa

University of Pennsylvania

Wanxin Jin

Arizona State University

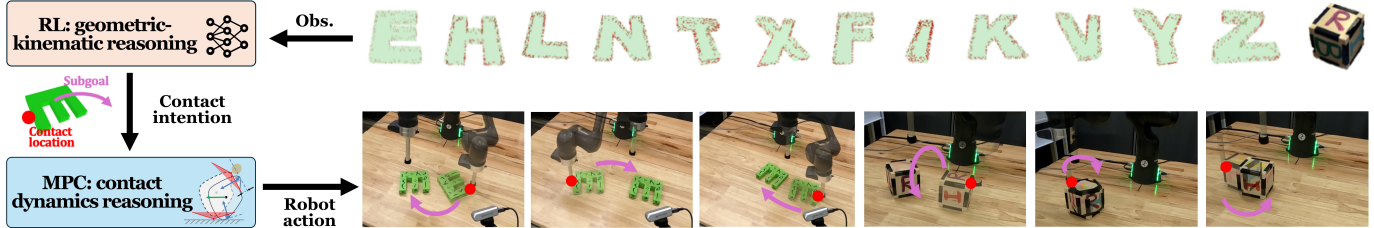


Fig. 1: Overview of our hierarchical RL-MPC framework for geometry-aware, long-horizon non-prehensile manipulation. A shared high-level RL policy performs geometric-kinematic reasoning and predicts a contact intention (object-surface contact locations and a post-contact object-level subgoal) across diverse non-convex geometries and tasks. Conditioned on it, a lower-level contact-implicit MPC performs contact dynamics reasoning locally, computing robot actions that realize the contact intention.

**Abstract**—A key challenge in contact-rich dexterous manipulation is the need to jointly reason over geometry, kinematic constraints, and intricate, nonsmooth contact dynamics. End-to-end visuomotor policies bypass this structure, but often require large amounts of data, transfer poorly from simulation to reality, and generalize weakly across tasks/embodiments. We address those limitations by leveraging a simple insight: dexterous manipulation is inherently hierarchical—at a high level, a robot decides where to touch (geometry) and move the object (kinematics); at a low level it determines how to realize that plan through contact dynamics. Building on this insight, we propose a hierarchical RL-MPC framework in which a high-level reinforcement learning (RL) policy predicts a contact intention, a novel object-centric interface that specifies (i) an object-surface contact location and (ii) a post-contact object-level subgoal pose. Conditioned on this contact intention, a low-level contact-implicit model predictive control (MPC) optimizes local contact modes and replans with contact dynamics to generate robot actions that robustly drive the object toward each subgoal. We evaluate the framework on non-prehensile tasks, including geometry-generalized pushing and object 3D reorientation. It achieves near-100% success with substantially reduced data (10× less than end-to-end baselines), highly robust performance, and zero-shot sim-to-real transfer.

## I. INTRODUCTION

Dexterous manipulation is a hallmark skill of intelligent robots. Recent research has made significant progress by training robot policies either from demonstrations, e.g., imitation learning [65, 8] and vision language action model [4, 26, 15], or from robot experience, e.g., reinforcement learning [42, 63]. These approaches typically learn a end-to-end policy from robot observations to low-level motor commands. While end-to-end methods can achieve impressive performance, such as emergent generalization [51] and robustness [31], they often face practical challenges, such as data scarcity, sim-to-real gap, and lack of task or embodiment generalizability.

Yet, human manipulation does not necessarily use a mono-

lithic end-to-end motor policy [37, 17]. For instance, when picking up a hammer to strike a nail, we do not directly infer low-level finger-joint commands from raw perception. Instead, we reason hierarchically: at a higher level, we decide *where* to contact (e.g., grasping the handle) and *what* object-level outcome to achieve (e.g., aligning the head with the nail); at lower level, we determine *how* to realize this plan guided by our intuitive physics, leveraging interaction strategies such as rolling, sliding, sticking, and disengagement. This hierarchical decomposition enables humans to combine semantic and geometric understanding and physics intuition, yielding efficient and robust manipulation control.

In this work, we propose an analogous hierarchical reasoning framework for robotic contact-rich manipulation. The hierarchical framework includes

- **Higher level: geometric-kinematic reasoning.** Given a scene observation, the higher-level learning-based policy determines where on the object surface the robot should establish contact (geometry) and where the object should move as a result (kinematics). To formalize this decision, we introduce a novel representation, termed **Contact Intention**, which specifies (i) contact locations on the object surface and (ii) a post-contact object subgoal for the desired object-level motion progress. We train this higher-level policy using reinforcement learning
- **Lower level: contact dynamics reasoning.** Conditioned on the generated contact intention, the dynamic contact planner generates joint-level commands by optimizing with contact dynamics. Leveraging recent advances in real-time contact-implicit model predictive control, this level synthesizes local contact modes, including rolling, sticking, sliding, and purposeful disengagement, at the suggested contact location, robustly moving the object to the planned subgoal.

The two levels forms a hierarchical RL–MPC framework that offers the following benefits:

(I) Significant data efficiency for geometry-aware long-horizon manipulation. By delegating contact dynamics reasoning to MPC optimization, the framework avoids inefficient learning over non-smooth contact dynamics. This allows the learning policy to focus on geometry and kinematics, enabling more efficient learning of long-horizon contact behaviors.

(II) Robust performance enabled by contact implicit MPC. The low-level MPC replans at high frequency ( $\sim 100$  Hz) with contact dynamics, continuously correcting for disturbances and modeling errors. This reduces sensitivity to simulation imperfections and improves robustness in sim-to-real deployment.

(III) Contact intention interface facilitating sim-to-real transfer. The contact-intention interface decouples the geometric-kinematic reasoning from low-level contact dynamics. This allows training a policy in simulator where geometry/kinematics transfer more reliably than contact dynamics. It makes the learned higher-level RL policy inherently more robust for sim-to-real deployment than an end-to-end policy that must account for hard-to-model contact dynamics.

In sum, we highlight our following contributions:

(1) We introduce *contact intention*, a hierarchical policy interface that decomposes dexterous manipulation into geometric–kinematic reasoning (where to touch) and contact dynamics reasoning (how to contact). It enables data-efficient, geometry-aware manipulation with robust sim-to-real transfer.

(2) We develop a hierarchical RL–MPC framework built on the contact intention interface. The higher-level RL policy predicts the contact intention, which then parameterizes a lower-level MPC for contact dynamics reasoning. This framework demonstrated state-of-the-art performance in data efficiency, success rate, robustness for geometry-aware long-horizon non-prehensile manipulation.

(3) We introduce multiple design novelties for higher-level RL policy training, including (i) a *tri-component* object-centric representation space that jointly encodes object geometry, task progress, and collision feasibility, and (ii) a *dual-branch* policy network architecture that captures both local geometry and global kinematic context. These designs enable a *unified* policy to learn non-prehensile manipulation across diverse objects and to generalize to unseen geometries.

## II. RELATED WORKS

### A. RL-MPC Hierarchy in Robot Manipulation

The use of RL–MPC architectures is extensive in robotic locomotion [61, 64, 6, 23, 19], where the primary objective is to achieve agile, adaptive, and diverse motor behaviors by combining learned high-level decision making with model-based control. This paradigm has more recently been transferred to robotic manipulation, where adaptability and generalization are crucial. For instance, in [47, 33], reinforcement learning is employed to infer the latent dynamics of deformable objects, which are subsequently incorporated into MPC or adaptive control for accurate manipulation. Other works [40, 34] leverage RL to assist with learning contact-rich dynamics models

and to provide a policy warm-start for sampling-based MPC solvers. In another line of research [3, 68], RL predicts intermediate end-effector goals that are tracked by a low-level MPC controller, thereby ensuring feasibility and safety during contact-rich tasks. Unlike prior uses of RL as auxiliary guidance or trajectory prediction, we introduce a tightly coupled RL–MPC hierarchy enabled by a novel *contact intention* interface for contact-rich manipulation. This design allows RL to reason over object geometry and kinematics while MPC handles high-frequency dynamic contact strategies, together enabling robust and dexterous manipulation.

### B. Non-Prehensile Manipulation

Since the proposed method is primarily applied to non-prehensile manipulation, we review the relevant prior work below. Non-prehensile manipulation [36] is defined as manipulating objects without explicitly grasping them. Classic work in non-prehensile manipulation studied the mechanics and control of the manipulator-object motion primitives [35, 1]. However, motion primitives face scalability issue in the open-ended world. Recent effort attacks the problem through contact-implicit planning [38, 39, 62, 55, 41, 7, 27, 2, 60, 5], which allows a robot to automatically discover contact modes through optimization with contact dynamics. Learning methods have also been used in non-prehensile manipulation, such as the work based on reinforcement learning [66, 9, 10, 29, 32], imitation learning [8, 45, 67, 44, 53, 54] or both [49]. From method structure perspective, our work is most relevant to the recent work of PushAnything [5], HiDex [7], HACMan [66] and HDP [54]. PushAnything samples contact locations and evaluates them via MPC; HiDex uses MCTS for contact selection followed by path planning; HACMan jointly learns contact selection and motion in a single RL policy; and HDP employs a diffusion-based hierarchy for contact prediction and trajectory generation. In contrast, our method introduces a tightly coupled RL–MPC hierarchy in which the learned decision goes beyond contact point selection to include an object-level subgoal, and the predicted contact intention directly parameterizes the low-level MPC controller.

### C. Robot Manipulation Based on Affordance

Our work is also related to affordance-based manipulation, where affordance describes which object-surface regions are suitable for interaction with the robot. Substantial research has focused on predicting and leveraging affordance maps for grasping tasks [18, 16, 57, 11, 12, 24, 28]. Recently, foundation models with strong semantic reasoning have further been used to infer affordance for robotic tasks [21, 22, 50, 30, 48, 52]. Affordance prediction alone only indicates *where* to make contact and lacks guidance on *how* to act after contact, while remaining static during manipulation. Our method addresses this by dynamically predicting contact intentions online and coupling them with a physics-based planner to generate adaptive, physically grounded non-prehensile motions.

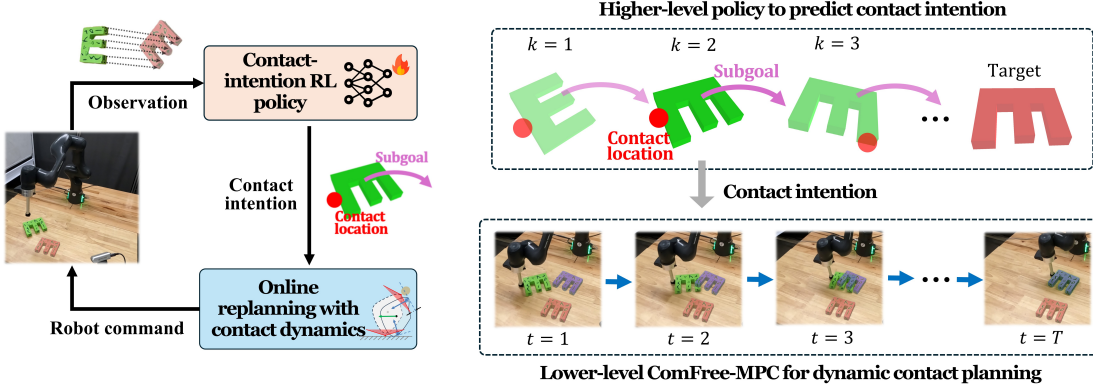


Fig. 2: Illustration of the RL-MPC hierarchical framework

### III. CONTACT INTENTION AND HIERARCHICAL RL-MPC FRAMEWORK

#### A. Contact Intention for Contact-Rich Manipulation

Consider  $n$  active contact points (general end effectors) on a robot that can be intentionally actuated to interact with an object. For example,  $n = 1$  for a robot arm with a stick-like end-effector, and  $n = 4$  for the fingertips of a four-fingered robotic hand. We distinguish these active contact points from passive ones that many arise without deliberate interaction, e.g., object–environment (or other robot links) contacts.

The goal of manipulation is for the robot to purposefully engage its  $n$  active contact points to interact with an object through contact and drive the object to a target pose  $\bar{q}^{\text{target}}$ . For this, we define **Contact Intention** as a higher-level action:

$$\mathbf{I} = (\bar{c}^1, \bar{c}^2, \dots, \bar{c}^n, \bar{q}^{\text{obj}}) \in \mathcal{G}^n \times \text{SE}(3), \quad (1)$$

Here,  $(\bar{c}^1, \bar{c}^2, \dots, \bar{c}^n)$  are the corresponding contact locations on the object surface. Each location  $\bar{c}^i \in \mathcal{G}$ ,  $i = 1, \dots, n$ , specifies an *interaction anchor* on the object surface  $\mathcal{G}$  for an active contact point  $i$  to engage with.  $\bar{q}^{\text{obj}} \in \text{SE}(3)$  is the post-contact subgoal pose of the object. It specifies the desired object-level outcome for the robot-object interaction at the suggested contact locations. The subgoal may not coincide with the final target  $\bar{q}^{\text{target}}$ ; it may be an intermediate object pose that provides meaningful progress toward  $\bar{q}^{\text{target}}$ . In this paper, we only consider non-prehensile manipulation using a stick-like end-effector attached to a robot arm. Thus,  $n = 1$ .

#### B. Overview of RL-MPC Hierarchical Framework

Our proposed RL-MPC hierarchical framework is shown in Fig. 2. It consists of a higher-level policy for object-centric geometry and kinematics reasoning and a lower-level policy for contact dynamics reasoning. The higher-level policy, trained using RL, predicts contact intention, which parameterizes the lower-level policy. The lower-level policy online optimize the robot action through local contact-implicit MPC.

a) *Higher-level RL policy for object-centric geometric-kinematic reasoning:* We formulate contact-intention prediction as a POMDP, where the action space  $\mathcal{A}$  is the proposed contact intention space  $\mathcal{A} = \mathcal{G}^n \times \text{SE}(3)$ . A higher-level policy  $\pi$  maps observations to contact intentions, which are

executed by the lower-level MPC. At each decision step  $k$ , the policy gets an observation  $\mathbf{o}_k$  and predicts contact intention  $\mathbf{I}_k = \pi(\mathbf{o}_k) \in \mathcal{A}$ . The predicted  $\mathbf{I}_k$  will parameterize the lower-level MPC for local contact dynamics reasoning. We train  $\pi$  in simulation, which will be detailed in Section VI.

b) *Lower-level contact-implicit MPC for contact dynamics reasoning:* For contact dynamics reasoning, we use the complementarity-free model predictive control (ComFree-MPC) for its robustness and high speed [25]. Given a contact intention  $\mathbf{I}_k = (\bar{c}_k^1, \bar{c}_k^2, \dots, \bar{c}_k^n, \bar{q}_k^{\text{obj}})$  from the higher level, ComFree-MPC reasons about the rich local contact strategies at the suggested contact location  $(\bar{c}_k^1, \bar{c}_k^2, \dots, \bar{c}_k^n)$  to move the object towards the subgoal  $\bar{q}_k^{\text{obj}}$ . Specifically, at each MPC step  $t$ , ComFree-MPC predicts  $H$  steps ahead through complementarity-free contact dynamics and optimizes the best robot action sequence for moving the object to the subgoal  $\bar{q}_k^{\text{obj}}$ . The optimization is written as

$$\begin{aligned} \min_{\mathbf{u}_{0:H-1}} \quad & \sum_{t=0}^{H-1} \sum_i L(\mathbf{p}_t^{\text{ee},i}, \bar{c}_k^i) + V(\mathbf{q}_H^{\text{obj}}, \bar{q}_k^{\text{obj}}) \\ \text{s.t.} \quad & \mathbf{x}_{t+1} = \text{ComFree}(\mathbf{x}_t, \mathbf{u}_t), t = 0, 1, \dots, H-1 \\ & \text{Given } \mathbf{x}_0 = \mathbf{x}^{\text{env}} \end{aligned} \quad (2)$$

Here,  $\mathbf{x}_{0:H}$  is the state of the manipulation system (robot and object).  $\mathbf{u}_{0:H-1}$  is the robot action input sequence, which is the desired displacement of the active contact points in Cartesian space. The MPC objective includes: (1) a running cost  $L$  which encourages the robot's active contact points  $(\mathbf{p}_t^{\text{ee},i})_{i=1}^n$  to get close to the suggested locations  $(\bar{c}_k^i)_{i=1}^n$ . (2) The terminal cost  $V$  encourage the robot to move the object  $\mathbf{q}_H^{\text{obj}}$  (at the prediction step  $H$ ) to the subgoal  $\bar{q}_k^{\text{obj}}$ . ComFree is the complementarity-free contact physics model, enabling fast receding horizon optimization.  $\mathbf{x}_0$  is set as the system's current physical state at each MPC call. After solving the optimization, only the first control input is sent as the action command to the robot. More details will be given in Section V.

c) *Multi-Rate RL-MPC Coupling:* The ComFree-MPC executes for  $T$  environment steps while the contact intention from the higher-level policy remains fixed. Below, we use  $k$  to denote the higher-level decision step for updating contact intentions and  $t$  to denote the lower-level MPC control step.

#### IV. RL FOR GEOMETRIC-KINEMATIC REASONING

We use RL to train the higher-level policy for geometric-kinematic reasoning. At each decision step, the policy receives an observation and outputs a contact intention. To enable effective policy learning, we design the observation and action spaces, reward, and policy architecture in this section.

##### A. RL Observation Space Design

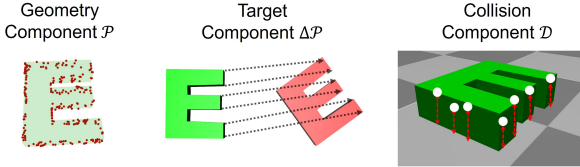


Fig. 3: Illustration of the geometric, target and collision components in RL observation space. The green mesh stands for current object pose, and the red mesh stands for the manipulation target.

As in Fig. 3, we design the higher-level observation space as a *tri-component, object-centric* representation that jointly encodes object geometry, task progress, and collision. This design enables the RL policy to reason about *object shape*, *task progress*, and *contact feasibility* in a unified manner.

a) *Geometry component*: We downsample a set of  $N$  keypoints  $\mathcal{P} = \{\mathbf{p}_i\}_{i=0}^{N-1}$  from object point cloud, defined in the *object frame*. These keypoints serve dual purposes: (i) as an approximation for the object geometry  $\mathcal{G}$ , and (ii) as discrete candidates for selecting contact location in contact intention, i.e.,  $(\bar{\mathcal{C}}_k^1, \bar{\mathcal{C}}_k^2, \dots, \bar{\mathcal{C}}_k^n) \subseteq \mathcal{P}$ .

b) *Target component*: To encode the target-aware observation, we define the *keypoint goal flow* in the object frame,  $\Delta\mathcal{P}_k = \{\delta_{i,k} | \delta_{i,k} = \mathbf{p}_{i,k}^{\text{target}} - \mathbf{p}_i\}_{i=0}^{N-1}$ , where  $\mathbf{p}_{i,k}^{\text{target}}$  denotes the position of the same keypoint  $\mathbf{p}_i$  when the object is at the target, expressed in the current object frame at decision step  $k$ . The keypoint goal flow  $\Delta\mathcal{P}_k$  represents the object-frame displacement of all keypoints from the current object pose to the target. Encoding keypoint goals in the object frame is crucial for stable and geometry-consistent policy learning. Otherwise, the discrepancy between body and world frames would force the policy to implicitly learn object translations and rotations, significantly increasing the learning burden.

c) *Collision component*: To inform contact feasibility, we include *per-keypoint clearance distances* as part of the observation. For each keypoint  $\mathbf{p}_i$  at decision step  $k$ , we compute its minimum Euclidean distance  $d_{i,k}$  to the environment (e.g., ground and walls). We collect these distances as  $\mathcal{D}_k = \{d_{i,k}\}_{i=0}^{N-1}$ .  $\mathcal{D}_k$  encode the *contact feasibility* of each keypoint: keypoints with small clearance ( $d_{i,k} \approx 0$ ) indicate it is in contact with their surrounding environment, thus are treated as invalid candidates to be a contact location. Including  $\mathcal{D}_k$  enables RL policy to avoid selecting contact locations that are physically blocked by the environment. For example, for a cube resting on a table, keypoints on the bottom face are infeasible contact locations for the end-effectors.

In sum, the tri-component, object-centric observation at the higher-level decision step  $k$  is the tuple

$$\mathbf{o}_k = (\mathcal{P}, \Delta\mathcal{P}_k, \mathcal{D}_k). \quad (3)$$

We provide the ablation and comparison study for our above design in Section VII.

##### B. RL Action Space Design

The higher-level RL policy receives the observation  $\mathbf{o}$  and selects a contact intention  $\mathbf{I} = (\bar{\mathcal{C}}^1, \bar{\mathcal{C}}^2, \dots, \bar{\mathcal{C}}^n, \bar{\mathbf{q}}^{\text{obj}})$ . Here, each contact location is selected from the keypoint set  $\mathcal{P}$ , i.e.,  $\bar{\mathcal{C}}^i \in \mathcal{P}, i = 1, 2, \dots, n$ .

Instead of predicting object subgoals in  $\text{SE}(3)$ , which is often inefficient for RL exploration to make meaningful progress toward the final goal, the higher-level RL policy selects MPC weights ( $w_{\text{pos}}, w_{\text{ori}}$ ) to implicitly define the subgoal:

$$V(\mathbf{q}^{\text{obj}}, \bar{\mathbf{q}}^{\text{obj}}) = w_{\text{pos}} e_{\text{pos}}(\mathbf{p}^{\text{obj}}, \bar{\mathbf{p}}^{\text{target}}) + w_{\text{ori}} e_{\text{ori}}(\mathbf{r}^{\text{obj}}, \bar{\mathbf{r}}^{\text{target}}), \quad (4)$$

where  $e_{\text{pos}}$  and  $e_{\text{ori}}$  measure the object's position and orientation errors to the final target. In the simplest case,  $(w_{\text{pos}}, w_{\text{ori}}) \in \{(1, 0), (0, 1), (1, 1)\}$  determines the subgoal to be target position-only, orientation-only, or exactly target itself, respectively. We use discrete sets  $\mathcal{W}_{\text{pos}} \times \mathcal{W}_{\text{ori}}$  to express richer trade-offs. In sum, the higher-level RL policy predicts

$$(\bar{\mathcal{C}}^1, \bar{\mathcal{C}}^2, \dots, \bar{\mathcal{C}}^n, w_{\text{pos}}, w_{\text{ori}}) = \pi(\mathbf{o}). \quad (5)$$

##### C. RL Reward

We train the higher-level RL policy using a reward

$$r_k = (w_1 r_{\text{dense}} + w_2 r_{\text{target}})(1 + r_{\text{feasible}}) + w_3 r_{\text{feasible}}, \quad (6)$$

where  $w_1, w_2, w_3$  are the weights for the negative dense keypoint flow reward ( $r_{\text{dense}} = -\frac{1}{N} \sum_{\delta_{i,k} \in \Delta\mathcal{P}_k} \|\delta_{i,k}\|$ ), sparse target-reaching reward ( $r_{\text{target}} = 1$  at final target), and negative contact feasibility reward  $r_{\text{feasible}} = -1$  when the contact location is invalid (e.g., contact location on the bottom surface); otherwise  $r_{\text{feasible}} = 0$ .

##### D. Architecture of RL Policy Network

Our higher-level RL policy is trained using an actor-critic framework. The policy network architecture is shown in Fig. 4, which adopts a *dual-branch design*. At decision step  $k$ , the policy network takes as input per-keypoint observations  $\mathbf{o}_k = \{\mathbf{p}_i, \delta_{i,k}, d_{i,k}\}_{i=0}^{N-1}$ , which encode each keypoint's body-frame location, goal displacement, and contact feasibility.

The input first goes through **geometric branch**: it processes per-keypoint features using a segmentation-style PointNet++ encoder to produce latent features  $\mathbf{z}_i$ , which are mapped to logits for contact location selection. Meantime, the input also goes through **global kinematic branch**, which aggregates all keypoint inputs into a single object-centric embedding  $\mathbf{g}$  via a classification-style PointNet++ encoder. Linear heads then predict categorical logits over MPC cost weights ( $\mathcal{W}_{\text{pos}}, \mathcal{W}_{\text{ori}}$ ) and a scalar value estimate for critic learning. This architecture efficiently combines local geometric reasoning with global object-level context, enabling the policy to select feasible contact locations and implicitly specify object subgoals.

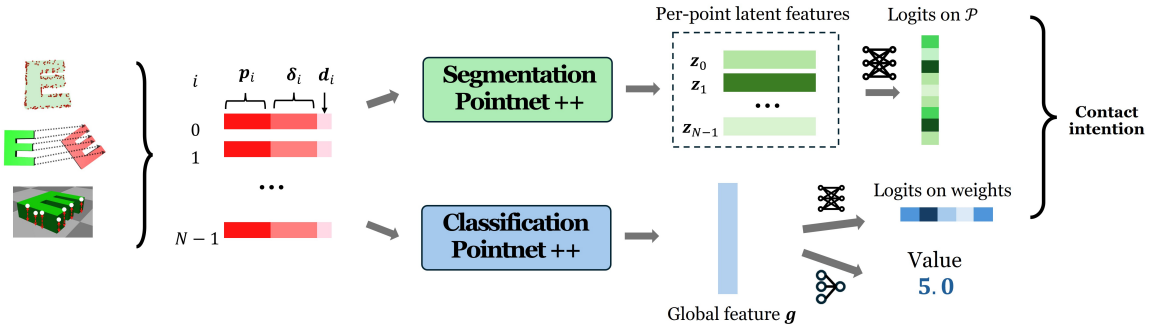


Fig. 4: The dual-branch architecture design for the higher-level RL policy that predicts contact intention.

## V. MPC FOR LOCAL DYNAMIC CONTACT PLANNING

We use ComFree-MPC for lower-level contact dynamics reasoning, conditioned on RL-predicted contact intentions. By leveraging an efficient closed-form contact physics model, ComFree-MPC performs high-speed receding-horizon optimization, enabling the system to reason over contact strategies (rolling, sliding, sticking, and making/breaking) and drive the object toward the subgoal. We detail the formulation below.

### A. Complementarity-Free Contact Dynamics

We adopt the quasi-dynamic complementarity-free contact model from [25] for our relatively slow non-prehensile manipulation task, given by

$$M\mathbf{v}^+ = h\boldsymbol{\tau}(\mathbf{u}) + h\tilde{J}^\top \boldsymbol{\lambda}, \quad (7)$$

$$\boldsymbol{\lambda} := \max\left(-K(h^2\tilde{J}M^{-1}\boldsymbol{\tau}(\mathbf{u}) + \tilde{\phi}), 0\right),$$

where  $h$  is the time step and  $\mathbf{v}^+$  is the next-step system velocity.  $M = \text{diag}(M_o, M_r)$  is the mass matrix, with object inertia  $M_o$  and robot stiffness  $M_r = h^2\text{diag}(K_r, \dots, K_r)$  for  $n$  active contact points. The force vector  $\boldsymbol{\tau}(\mathbf{u}) = [\boldsymbol{\tau}_o, \boldsymbol{\tau}_r(\mathbf{u})]$  includes robot gravitational force  $\boldsymbol{\tau}_o$  and robot actuation force  $\boldsymbol{\tau}_r(\mathbf{u})$ . We assume robot is in operational space impedance control and moves slowly. Thus, its damping and inertial effects are neglected, and end-effector force can be approximated as a spring model with stiffness  $K_r$ :  $\boldsymbol{\tau}_r(\mathbf{u}) = K_r\mathbf{u}$ . Here, the input  $\mathbf{u}$  is desired end-effector displacement. The contact-force vector  $\boldsymbol{\lambda}$  is produced by a spring-damper model on the dual cones of the Coulomb friction cones, with  $\tilde{J}$  and  $\tilde{\phi}$  the Jacobian and signed distances for all candidate dual cones, and  $K$  the dual-cone stiffness. Different contact modes, e.g., sticking, sliding, and separation, is captured by different penetration regimes across facets of the dual cones.

With  $\mathbf{v}^+$ , the state after one-step forwarding of the contact dynamics is  $\mathbf{x}^+ = \mathbf{x} \oplus h\mathbf{v}^+$ , where  $\oplus$  stands for the integration of system positions with velocities. The details of this closed-form contact model can be found in [25].

### B. MPC Cost Function

In the ComFree-MPC (2), the *running cost* is defined as

$$\sum_{i=1}^n L(\mathbf{p}_t^{\text{ee},i}, \bar{\mathbf{c}}_k^i) = \sum_{i=1}^n w_c \|\mathbf{p}_t^{\text{ee},i} - T_{\text{obj}}^w \bar{\mathbf{c}}_k^i\|^2, \quad (8)$$

where  $T_{\text{obj}}^w$  transforms  $\bar{\mathbf{c}}^i$  to the world frame.  $w_c$  is the hyperparameter controlling the strength of this cost. This is

to encourage the robot end-effectors to stick to the contact locations from the contact intention. The terminal cost follows the reparameterization form (4), with

$$V = w_{\text{pos}} \|\mathbf{p}_H^{\text{obj}} - \bar{\mathbf{p}}^{\text{target}}\|^2 + w_{\text{ori}} (1 - \langle \mathbf{r}_H^{\text{obj}}, \bar{\mathbf{r}}^{\text{target}} \rangle^2), \quad (9)$$

where  $\mathbf{p}_H^{\text{obj}}, \mathbf{r}_H^{\text{obj}}$  are respectively the position and quaternion in predicted object pose  $\mathbf{q}_H^{\text{obj}}$ .  $\bar{\mathbf{p}}^{\text{target}}, \bar{\mathbf{r}}^{\text{target}}$  are the position and rotation component in  $\bar{\mathbf{q}}^{\text{target}}$ .

## VI. APPLICATION TO NON-PREHENSILE MANIPULATION

We apply our framework to solve two representative non-prehensile manipulation tasks: *geometry-generalized pushing* and *object 3D reorientation*. Both tasks are performed with a 7-DOF Franka robot arm with a stick end-effector (Fig. 5).



Fig. 5: Two non-prehensile manipulation tasks. Left: Geometry-generalized pushing. Right: object 3D reorientation.

### A. Task Setup

a) *Geometry-generalized pushing*: The goal is to learn a *unified policy* that pushes diverse letter-shaped objects from arbitrary initial poses to planar targets. We use 12 English letters (Fig. 1): (E, H, L, N, T, X) for training and (F, I, K, V, Y, Z) held out for generalization test. The task requires long-horizon contact reasoning: sequentially switching contact facets and selecting appropriate contact strategies. Letters vary geometrically, from elongated (I) to branched shapes (K, Y), providing a challenging benchmark for geometry-aware contact-rich manipulation. For each letter, 256 keypoints are uniformly sampled on vertical side surfaces (Fig. 1).

b) *Object 3D reorientation*: The goal is to reorient a cube from a random initial pose to a random 3D target. We uniformly sample 256 keypoints on its six faces. This task evaluates the method's ability to generate richer contact strategies for precise 3D reorientation beyond planar pushing.

The detailed task settings for both the simulation and real world system can be found in Appendix IX-A.

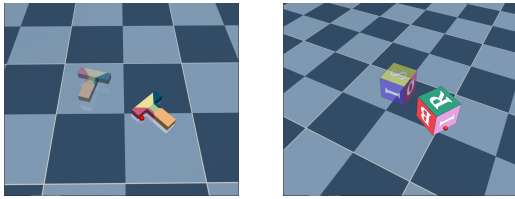


Fig. 6: In the higher-level RL policy training, an abstract end-effector (red dot) replaces full robot arm. The target is half-transparent.

### B. Training Higher-Level Robot-Abstract Policy in Simulation

The higher-level contact-intention policy predicts object-centric contact locations and kinematic subgoals, so we train it in a simulation environment where the robot end-effector is abstracted a mass–spring–damper point (Fig. 6). This reduces lower-level MPC complexity, speeding up learning. Despite the notable model gaps, we will later show that our decoupled hierarchical framework enables the trained policy to direct transfer to full robot embodiments in simulation (Section VII) and real experiments (Section VIII) with lower-level MPC.

We train the higher-level policy using PPO [46]. At each episode, object and target poses are randomized (Appendix IX-A), with one training object sampled per episode for the geometry-generalized pushing task. Episodes end on success or after 64 steps. Details on rewards, hyperparameters, and implementation are in Appendix IX-B.

### C. Zero-Shot Transfer to Full Robotic Systems

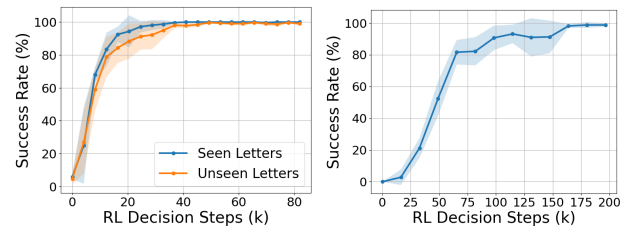
Deploying the trained higher-level contact-intention policy on a full robot requires adding the robot-specific ComFree-MPC. For one decision step of the RL policy, the lower-level ComFree-MPC moves the robot end effector near the desired contact location and executes dynamic contact replanning and control for multiple control steps. Since the MPC objective is parameterized by the policy, no additional training is needed. Three MPC parameter sets, tuned for simulation, real-world pushing, and real-world 3D reorientation, account for different dynamics; details are in Appendix IX-C.

## VII. SIMULATION RESULTS

### A. Learning Curves

1) *Training in robot-abstract setting*: We perform five independent training runs per task, evaluating success rates at saved checkpoints with 64 trials each. In geometry-generalized pushing, we report separate curves for seen and unseen letters, randomly sampling objects and start/target poses per trial. For object 3D reorientation, trials are generated similarly. A trial succeeds if the object reaches sufficiently close to the target within 64 RL steps. Pose distributions and success criteria are in Appendix IX-A, and learning curves with the abstract end-effector are shown in Fig. 7.

The results show that the proposed method achieves high success rates with relatively small amount of training data:  $100\% \pm 0\%$  for seen and  $99.06\% \pm 1.25\%$  for unseen letters in pushing, and  $98.75\% \pm 1.17\%$  for 3D reorientation, after  $\sim 40k$  and  $\sim 100k$  RL steps, respectively. The near-overlap of pushing



(a) Geometry-generalized pushing (b) Object 3D reorientation

Fig. 7: Learning curves for both tasks.

learning curves for seen and unseen objects also indicates strong generalization to novel geometries in the pushing task.

2) *Evaluation in Full Robotic System*: We further evaluate the trained policies in a full Franka-arm simulation environment. For each trained checkpoint, we run 5 evaluation trials per letter in the geometry-generalized pushing task and 20 evaluation trials in the object 3D reorientation task. The learned policies achieve consistently high success rates (near 100%) while requiring only a small number of high-level RL decision steps to complete each task (approximately 10 on average). Table I summarizes the success rates of our method in both the abstract and full-system settings, along with the number of RL decision steps required for task completion in full-system setting. We denote the pushing and 3D reorientation tasks by “P” and “R”, respectively.

TABLE I: Result in Simulated Abstract and Full robot Setting

Task	Success (Abstract)	Success (Full)	Steps (Full)
P (seen)	$100\% \pm 0\%$	$100\% \pm 0\%$	$9.0 \pm 5.4$
P (unseen)	$99.06\% \pm 1.25\%$	$97.34\% \pm 2.5\%$	$11.2 \pm 8.0$
R	$98.75\% \pm 1.17\%$	$100\% \pm 0\%$	$14.0 \pm 9.5$

### B. Baseline Comparison

We compare our hierarchical RL-MPC method with two baselines: (i) a end-to-end RL policy and (ii) a HACMan-style hierarchical policy without a physics-based MPC layer. In each comparison, five independent training runs are performed, and performance is evaluated using 64 trials per run.

a) *Comparison with End-to-end RL learning*: The end-to-end policy directly predicts end-effector actions, using an observation that includes object keypoints, goal flow, per-point clearance, and end-effector flow (distance vectors between the end-effector and all keypoints), all in world frame. End effector flow provides spatial context about the robot–object geometry. The policy reuses the global kinematic branch (Section IV-D) with separate linear heads for action and value prediction.

We found that directly using the reward in Section IV-C leads to the struggling of the end-to-end policy to effectively explore the effect contact with the object. To facilitate object interaction, we add an additional reward term  $0.5 \exp(-\|d_{\text{obj,ee}}\|^2 / 0.02)$ , to encourage the end effector to approach the object, where  $d_{\text{obj,ee}}$  denotes the distance between the end effector and the object center. Episodes are also terminated early when  $\|d_{\text{obj,ee}}\| \geq 0.25$ , with a penalty of  $-5$ , to discourage drifting away from the object.

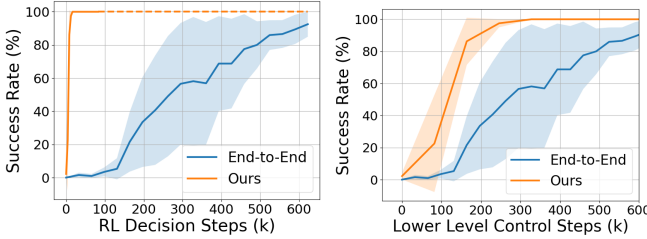


Fig. 8: The result of baseline comparison with the end-to-end RL. Left: the training curve with respect to RL decision steps. Right: the training curve with respect to lower-level control steps.

We evaluate the end-to-end and our hierarchical policies on (1) sample efficiency and (2) robustness to environment variations (i.e., sim-to-sim transfer), including external forces, friction, and actuator variations (Appendix IX-D). Ours use the same lower-level ComFree-MPC in geometry-generalized pushing task without additional tuning.

Fig. 8 shows checkpoint success versus high-level RL steps and total end-effector commands. The end-to-end policy converges slowly, reaching  $92.5\% \pm 7.55\%$  after  $\sim 600K$  RL steps (corresponding to  $600K$  control steps), while our proposed method achieves  $100\% \pm 0\%$  in  $15K$  steps (approximately  $300K$  control steps), giving  $\sim 40\times$  improvement in terms of RL decision steps and  $\sim 2\times$  with respect to control steps.

The evaluation results of robustness to environment variation is shown in Table II. While the end-to-end policy performs well under external force and friction variations, its success drops from  $92.5\%$  to  $44.0\%$  under robot actuator variations (including actuator's stiffness and damping) due to overfitting to nominal dynamics in training. In contrast, the hierarchical policy maintains  $100\% \pm 0\%$  success rate. We attribute this robustness to two factors: the higher-level contact-intention policy abstracts away low-level dynamics variations, and the lower-level MPC performs high-frequency replanning with an explicit physics model, continuously correcting execution errors induced by model errors. Overall, these results indicate that the proposed hierarchy simplifies learning and substantially improves robustness in environment variations.

TABLE II: Evaluation results for robustness to environment variations

Variations	Success Rate (End-to-End)	Success Rate (Ours)
No Perturbation	$92.5\% \pm 7.55\%$	$100\% \pm 0\%$
External Force	$89.6\% \pm 8.6\%$	$100\% \pm 0\%$
Friction	$92.8\% \pm 6.8\%$	$100\% \pm 0\%$
Actuation	$44.0\% \pm 24.2\%$	$100\% \pm 0\%$

*b) Comparison with HACMan-Style Hierarchy:* We compare our RL-MPC framework with a HACMan-style hierarchical RL policy [66], which directly predicts contact locations and corresponding end-effector 3D displacements. The RL observation space is unchanged, while the action space is  $\mathcal{P} \times [-0.1, 0.1]^3$ , where  $\mathcal{P}$  denotes the set of candidate contact keypoints and  $[-0.1, 0.1]^3$  represents the end-effector 3D-displacement. Both our policy network are reused, but the MPC weight head is replaced with a displacement head. This comparison quantifies how the MPC lower-level aids structured exploration and improves manipulation success.

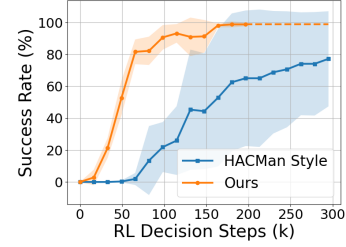


Fig. 9: Result of comparison with HACMan-style hierarchical policy.

The training result for solving the 3D object reorientation task is shown in Fig. 9. HACMan-style hierarchical policy requires roughly  $300K$  RL steps to reach about  $77.19\% \pm 29.80\%$  success rate, while our method converges to  $98.75\% \pm 1.17\%$  success rate within  $200K$  steps. Furthermore, the variance in performance increases considerably without the MPC layer. These results highlight that the MPC plays a critical role in ensuring consistency and stability during task execution.

### C. Ablation Studies

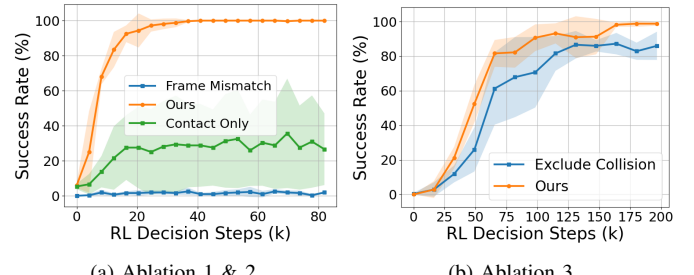


Fig. 10: Results of ablation studies.

*1) Ablation 1: Removing Subgoal Prediction:* To evaluate the role of *subgoal prediction*, we consider a variant where the higher-level policy predicts only contact locations, with fixed MPC terminal-cost weights (e.g.  $w_{\text{pos}}=100$ ,  $w_{\text{ori}}=4$ ) and all other settings unchanged. As shown by the green curve in Fig. 10(a), removing subgoal prediction drops the success rate from  $100\% \pm 0\%$  to  $26.56\% \pm 20.44\%$ . We find that in the contact-only case, the MPC must simultaneously minimize both positional and rotational errors, leading to inefficient pushing that often exceeds the 64-step episode limit.. The ablation result highlights the critical role of subgoal selection for efficient manipulation.

*2) Ablation 2: Frame Mismatch in Observation:* This ablation is designed to highlight the importance of expressing the geometry component  $\mathcal{P}$  and the target component  $\Delta\mathcal{P}$  in a consistent reference frame. We train a policy under the same settings as the main experiment in the geometry-generalized pushing task, with the only difference being that  $\Delta\mathcal{P}$  is expressed in the world while  $\mathcal{P}$  remains in the object frame. As shown with the blue curve in Fig. 10(a), learning fails to bootstrap under this mismatch. This result demonstrates that a consistent object-centric representation is crucial for stable learning and for enabling the policy to reason effectively about geometry and goal relationships.

3) *Ablation 3: Removing Collision Component in Observation:* To evaluate the role of the *collision component*  $\mathcal{D}_k$ , we remove it from the observation for *object 3D reorientation* task, keeping all other settings unchanged. As shown in Fig. 10(b), both learning speed and success rate drop (the success rate drops from  $98.75\% \pm 1.17\%$  to  $85.94\% \pm 8.15\%$ ). A possible explanation is that without collision information, the value network overfits the feasibility penalty  $r_{\text{feasible}}$ , implicitly associating it with particular object configurations or poses, rather than with true contact feasibility. Thus it introduces noise and degrades policy performance. This result highlights the importance of  $\mathcal{D}_k$  for effective manipulation.

### VIII. REAL-WORLD EXPERIMENT

#### A. Experiment Setup

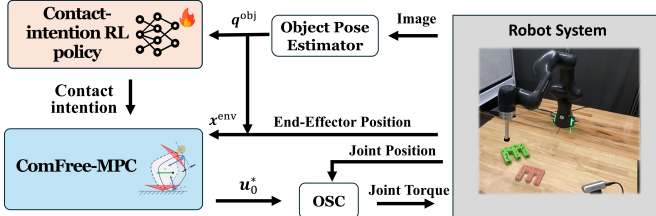


Fig. 11: The Diagram of real-world system.

We deploy the higher-level policy trained in simulation in Section VII on real-world system. Fig. 11 shows the hardware setup. The system composed of four modules. (1) The higher-level RL policy module. We use the stochastic version of the trained RL policy for contact-point selection in 3D reorientation task. This helps prevent the system from getting stuck due to noisy pose estimation. (2) Lower-level ComFree-MPC module ( $\sim 100\text{Hz}$ ). (3) Robot operational space control (OSC) stack ( $\sim 500\text{Hz}$ ) [13]. It receives the end-effector displacement command from ComFree-MPC. (4) The vision perception module ( $\sim 40\text{Hz}$ ), which uses the TwinTrack [59] and FoundationPose++ [56, 58]. These components interact through LCM communication middleware[20]. All objects are 3D-printed from the exact STL meshes used during training.

#### B. Results

We evaluate the proposed method on real-world geometry-generalized pushing and object 3D reorientation. For each letter in pushing task, we perform 10 independent trials. For the reorientation, we perform 25 independent trials. For each trial, the object is randomly placed on the table, and the target position is randomly generated. We analyze the result both qualitatively and quantitatively.

a) *Quantitative evaluation:* Table III shows the hardware results for each letter in the pushing task and cube 3D reorientation task. It reports using three metrics: success rate over a fixed number of trials, the wall-clock time for completing the task (exec\_time), and the number of RL decision steps needed to complete the task (num\_steps).

In the pushing tasks, most objects, including unseen ones, achieve 100% success with few steps, showing reliable sim-to-real transfer; only letter I occasionally fails due to tracking

TABLE III: Result in real-world non-prehensile manipulation

object	success_rate	exec_time (s)	num_steps
E	100.0%	$58.89 \pm 28.70$	$5.60 \pm 2.72$
F	100.0%	$89.64 \pm 67.31$	$8.70 \pm 6.53$
H	100.0%	$54.54 \pm 21.12$	$5.20 \pm 2.04$
I	70.0%	$72.69 \pm 31.53$	$7.14 \pm 2.91$
K	100.0%	$64.01 \pm 31.27$	$6.20 \pm 3.08$
L	100.0%	$100.39 \pm 42.01$	$9.60 \pm 3.89$
N	100.0%	$66.56 \pm 42.20$	$6.20 \pm 3.85$
T	100.0%	$48.13 \pm 27.50$	$4.70 \pm 2.71$
V	100.0%	$66.41 \pm 44.49$	$6.40 \pm 4.33$
X	100.0%	$54.62 \pm 31.23$	$5.30 \pm 3.06$
Y	100.0%	$93.64 \pm 41.15$	$9.00 \pm 3.92$
Z	100.0%	$68.25 \pm 66.42$	$6.60 \pm 6.24$
Cube	100.0%	$237.74 \pm 147.55$	$24.96 \pm 15.5$

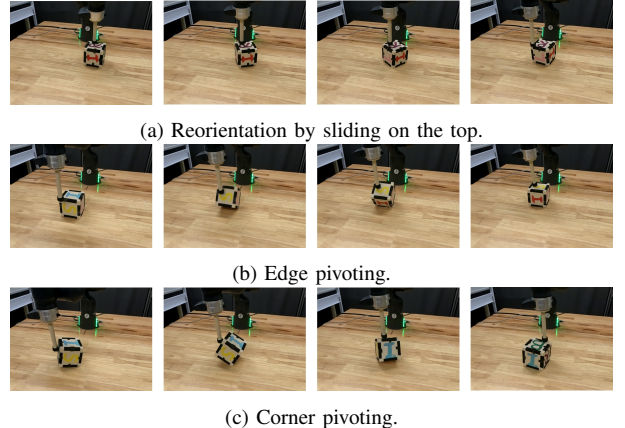


Fig. 12: Different contact strategies in the 3D reorientation experiment.

failure. In the 3D reorientation task, our method maintains strong success, though requiring more steps.

b) *Qualitative: diverse contact interaction strategies:* In the object 3D reorientation task, multiple contact interaction strategies emerge, shown in Fig. 12. In the first row, the robot's end effector reorientates the cube purely by frictional sliding on the top face. In the second row, the end effector pivots the cube at an edge to rotate the object. In the third row, the robot reorientates the cube by pivoting it at one corner. The diverse interaction demonstrate the policy's ability to adapt its contact strategy in different task situations, rather than relying on a single manipulation pattern. Overall, the results demonstrate that the hierarchical RL-MPC policy enables efficient, reliable, and generalizable real-world manipulation.

### IX. CONCLUSION AND LIMITATIONS

We introduced a hierarchical RL-MPC framework for contact-rich manipulation that explicitly separates geometric-kinematic planning from contact dynamics reasoning. The high-level RL policy predicts a *contact intention*, including an object-surface contact location and a post-contact object-level subgoal, while a low-level contact-implicit MPC replans contact modes online with contact dynamics to robustly execute each intention. Across non-prehensile manipulation tasks, our approach achieves near-100% success with substantially improved data efficiency less than baselines, strong robustness, and zero-shot sim-to-real transfer.

The proposed approach has two main limitations. First, it relies on accurate object pose estimation for computing goal flow and MPC terms. Second, using a discrete keypoint set  $\mathcal{P}$  simplifies learning but scales poorly with multiple end-effectors due to the combinatorial action space. Future work will explore perception-native planning and extend the interface to multi-finger manipulation for scalable multi-fingered dexterous manipulation.

## REFERENCES

[1] Srinivas Akella and Matthew T Mason. Posing polygonal objects in the plane by pushing. *The International Journal of Robotics Research*, 17(1):70–88, 1998.

[2] Alp Aydinoglu, Adam Wei, Wei-Cheng Huang, and Michael Posa. Consensus complementarity control for multi-contact mpc. *IEEE Transactions on Robotics*, 2024.

[3] Zhenshan Bing, Aleksandr Mavrichev, Sicong Shen, Xiangtong Yao, Kejia Chen, Kai Huang, and Alois Knoll. Safety guaranteed manipulation based on reinforcement learning planner and model predictive control actor. *arXiv preprint arXiv:2304.09119*, 2023.

[4] Kevin Black, Noah Brown, Danny Driess, Adnan Esmail, Michael Equi, Chelsea Finn, Niccolò Fusai, Lachy Groom, Karol Hausman, Brian Ichter, et al.  $\pi_0$ : A vision-language-action flow model for general robot control. *corr, abs/2410.24164*, 2024. doi: 10.48550. *arXiv preprint ARXIV.2410.24164*.

[5] Hien Bui, Yufei Yang Gao, Haoran Yang, Eric Cui, Siddhant Mody, Brian Acosta, Thomas Stephen Felix, Bibit Bianchini, and Michael Posa. Push anything: Single-and multi-object pushing from first sight with contact-implicit mpc. *arXiv preprint arXiv:2510.19974*, 2025.

[6] Yiyu Chen and Quan Nguyen. Learning agile locomotion and adaptive behaviors via rl-augmented mpc. In *2024 IEEE International Conference on Robotics and Automation (ICRA)*, pages 11436–11442. IEEE, 2024.

[7] Xianyi Cheng, Sarvesh Patil, Zeynep Temel, Oliver Kroemer, and Matthew T Mason. Enhancing dexterity in robotic manipulation via hierarchical contact exploration. *IEEE Robotics and Automation Letters*, 9(1):390–397, 2023.

[8] Cheng Chi, Zhenjia Xu, Siyuan Feng, Eric Cousineau, Yilun Du, Benjamin Burchfiel, Russ Tedrake, and Shuran Song. Diffusion policy: Visuomotor policy learning via action diffusion. *The International Journal of Robotics Research*, 44(10-11):1684–1704, 2025.

[9] Yoonyoung Cho, Junhyek Han, Yoontae Cho, and Beomjoon Kim. Corn: Contact-based object representation for nonprehensile manipulation of general unseen objects. *arXiv preprint arXiv:2403.10760*, 2024.

[10] Yoonyoung Cho, Junhyek Han, Jisu Han, and Beomjoon Kim. Hierarchical and modular network on nonprehensile manipulation in general environments. *arXiv preprint arXiv:2502.20843*, 2025.

[11] Fu-Jen Chu, Ruinian Xu, Landan Seguin, and Patricio A Vela. Toward affordance detection and ranking on novel objects for real-world robotic manipulation. *IEEE Robotics and Automation Letters*, 4(4):4070–4077, 2019.

[12] Fu-Jen Chu, Ruinian Xu, and Patricio A Vela. Learning affordance segmentation for real-world robotic manipulation via synthetic images. *IEEE Robotics and Automation Letters*, 4(2):1140–1147, 2019.

[13] Jean Elsner. Taming the panda with python: A powerful duo for seamless robotics programming and integration. *SoftwareX*, 24:101532, 2023. ISSN 2352-7110. doi: <https://doi.org/10.1016/j.softx.2023.101532>. URL <https://www.sciencedirect.com/science/article/pii/S2352711023002285>.

[14] Matthias Fey, Jinu Sunil, Akihiro Nitta, Rishi Puri, Manan Shah, Blaž Stojanović, Ramona Bendias, Barghi Alexandria, Vid Kocijan, Zecheng Zhang, Xinwei He, Jan E. Lenssen, and Jure Leskovec. PyG 2.0: Scalable learning on real world graphs. In *Temporal Graph Learning Workshop @ KDD*, 2025.

[15] AI Figure. Helix: A vision-language-action model for generalist humanoid control. *Figure AI News*, 2024.

[16] Yiran Geng, Boshi An, Haoran Geng, Yuanpei Chen, Yaodong Yang, and Hao Dong. End-to-end affordance learning for robotic manipulation. *arXiv preprint arXiv:2209.12941*, 2022.

[17] Scott T Grafton. The cognitive neuroscience of prehension: recent developments. *Experimental brain research*, 204(4):475–491, 2010.

[18] Tucker Hermans, James M Rehg, and Aaron Bobick. Affordance prediction via learned object attributes. In *IEEE international conference on robotics and automation (ICRA): Workshop on semantic perception, mapping, and exploration*, pages 181–184. Citeseer, 2011.

[19] Lei Hu, Liang Ding, Huaiguang Yang, Tie Liu, Ao Zhang, Siyang Chen, Haibo Gao, Peng Xu, and Zongquan Deng. Lno-driven deep rl-mpc: Hierarchical adaptive control architecture for dynamic legged locomotion. *IEEE Transactions on Industrial Informatics*, 2025.

[20] Albert S Huang, Edwin Olson, and David C Moore. Lcm: Lightweight communications and marshalling. In *2010 IEEE/RSJ International Conference on Intelligent Robots and Systems*, pages 4057–4062. IEEE, 2010.

[21] Wenlong Huang, Fei Xia, Dhruv Shah, Danny Driess, Andy Zeng, Yao Lu, Pete Florence, Igor Mordatch, Sergey Levine, Karol Hausman, et al. Grounded decoding: Guiding text generation with grounded models for embodied agents. *Advances in Neural Information Processing Systems*, 36:59636–59661, 2023.

[22] Yuheng Ji, Huajie Tan, Jiayu Shi, Xiaoshuai Hao, Yuan Zhang, Hengyuan Zhang, Pengwei Wang, Mengdi Zhao, Yao Mu, Pengju An, et al. Robobrain: A unified brain model for robotic manipulation from abstract to concrete. In *Proceedings of the Computer Vision and Pattern Recognition Conference*, pages 1724–1734, 2025.

[23] Muye Jia, Mingyuan Tao, Meng Xu, Peng Zhang, Jiayi Qiu, Gerald Bergsieker, and Jun Chen. Rl-mpc: rein-

forcement learning aided model predictive controller for autonomous vehicle lateral control. Technical report, SAE Technical Paper, 2024.

[24] Zhenyu Jiang, Yifeng Zhu, Maxwell Svetlik, Kuan Fang, and Yuke Zhu. Synergies between affordance and geometry: 6-dof grasp detection via implicit representations. *arXiv preprint arXiv:2104.01542*, 2021.

[25] Wanxin Jin. Complementarity-free multi-contact modeling and optimization for dexterous manipulation. *arXiv preprint arXiv:2408.07855*, 2024.

[26] Moo Jin Kim, Karl Pertsch, Siddharth Karamcheti, Ted Xiao, Ashwin Balakrishna, Suraj Nair, Rafael Rafailov, Ethan Foster, Grace Lam, Pannag Sanketi, et al. Openvla: An open-source vision-language-action model. *arXiv preprint arXiv:2406.09246*, 2024.

[27] Vince Kurtz, Alejandro Castro, Aykut Özgün Önol, and Hai Lin. Inverse dynamics trajectory optimization for contact-implicit model predictive control. *The International Journal of Robotics Research*, page 02783649251344635, 2023.

[28] Gen Li, Nikolaos Tsagkas, Jifei Song, Ruaridh Mon-Williams, Sethu Vijayakumar, Kun Shao, and Laura Sevilla-Lara. Learning precise affordances from egocentric videos for robotic manipulation. In *Proceedings of the IEEE/CVF International Conference on Computer Vision*, pages 10581–10591, 2025.

[29] Wenzuan Li, Hang Zhao, Zhiyuan Yu, Yu Du, Qin Zou, Ruizhen Hu, and Kai Xu. Pin-wm: Learning physics-informed world models for non-prehensile manipulation. *arXiv preprint arXiv:2504.16693*, 2025.

[30] Xiaoqi Li, Mingxu Zhang, Yiran Geng, Haoran Geng, Yuxing Long, Yan Shen, Renrui Zhang, Jiaming Liu, and Hao Dong. Manipllm: Embodied multimodal large language model for object-centric robotic manipulation. In *Proceedings of the IEEE/CVF Conference on Computer Vision and Pattern Recognition*, pages 18061–18070, 2024.

[31] Xiaoqi Li, Liang Heng, Jiaming Liu, Yan Shen, Chenyang Gu, Zhuoyang Liu, Hao Chen, Nuowei Han, Renrui Zhang, Hao Tang, et al. 3ds-vla: A 3d spatial-aware vision language action model for robust multi-task manipulation. In *9th Annual Conference on Robot Learning*, 2025.

[32] Toru Lin, Kartik Sachdev, Linxi Fan, Jitendra Malik, and Yuke Zhu. Sim-to-real reinforcement learning for vision-based dexterous manipulation on humanoids. *arXiv preprint arXiv:2502.20396*, 2025.

[33] Jiayi Liu, Sihang Yang, Yiwei Wang, Huan Zhao, and Han Ding. Autonomous bimanual manipulation of deformable objects using deep reinforcement learning guided adaptive control. In *2025 IEEE International Conference on Robotics and Automation (ICRA)*, pages 6904–6910. IEEE, 2025.

[34] Alexandre Lopes, Catarina Barata, and Plinio Moreno. Model-based lookahead reinforcement learning for in-hand manipulation. *arXiv preprint arXiv:2510.08884*, 2025.

[35] Kevin M Lynch and Matthew T Mason. Stable pushing: Mechanics, controllability, and planning. *The international journal of robotics research*, 15(6):533–556, 1996.

[36] Matthew T Mason. Mechanics and planning of manipulator pushing operations. *The International Journal of Robotics Research*, 5(3):53–71, 1986.

[37] Josh Merel, Matthew Botvinick, and Greg Wayne. Hierarchical motor control in mammals and machines. *Nature communications*, 10(1):5489, 2019.

[38] Igor Mordatch, Zoran Popović, and Emanuel Todorov. Contact-invariant optimization for hand manipulation. In *Proceedings of the ACM SIGGRAPH/Eurographics symposium on computer animation*, pages 137–144, 2012.

[39] Joao Moura, Theodoros Stouraitis, and Sethu Vijayakumar. Non-prehensile planar manipulation via trajectory optimization with complementarity constraints. In *2022 International Conference on Robotics and Automation (ICRA)*, pages 970–976. IEEE, 2022.

[40] Muhammad Omer, Rami Ahmed, Benjamin Rosman, and Sharief F Babikir. Model predictive-actor critic reinforcement learning for dexterous manipulation. In *2020 International Conference on Computer, Control, Electrical, and Electronics Engineering (ICCCEEE)*, pages 1–6. IEEE, 2021.

[41] Michael Posa, Cecilia Cantu, and Russ Tedrake. A direct method for trajectory optimization of rigid bodies through contact. *The International Journal of Robotics Research*, 33(1):69–81, 2014.

[42] Haozhi Qi, Ashish Kumar, Roberto Calandra, Yi Ma, and Jitendra Malik. In-hand object rotation via rapid motor adaptation. In *Conference on Robot Learning*, pages 1722–1732. PMLR, 2023.

[43] Antonin Raffin, Ashley Hill, Adam Gleave, Anssi Kanervisto, Maximilian Ernestus, and Noah Dormann. Stable-baselines3: Reliable reinforcement learning implementations. *Journal of Machine Learning Research*, 22(268):1–8, 2021. URL <http://jmlr.org/papers/v22/20-1364.html>.

[44] Quentin Rouxel, Andrea Ferrari, Serena Ivaldi, and Jean-Baptiste Mouret. Flow matching imitation learning for multi-support manipulation. In *2024 IEEE-RAS 23rd International Conference on Humanoid Robots (Humanoids)*, pages 528–535. IEEE, 2024.

[45] Yuki Saigusa, Sho Sakaino, and Toshiaki Tsuji. Imitation learning for nonprehensile manipulation through self-supervised learning considering motion speed. *IEEE Access*, 10:68291–68306, 2022.

[46] John Schulman, Filip Wolski, Prafulla Dhariwal, Alec Radford, and Oleg Klimov. Proximal policy optimization algorithms. *arXiv preprint arXiv:1707.06347*, 2017.

[47] Changyeob Shin, Peter Walker Ferguson, Sahba Aghajani Pedram, Ji Ma, Erik P Dutson, and Jacob Rosen. Autonomous tissue manipulation via surgical robot using learning based model predictive control. In *2019 International conference on robotics and automation (ICRA)*,

pages 3875–3881. IEEE, 2019.

[48] Zirui Song, Guangxian Ouyang, Mingzhe Li, Yuheng Ji, Chenxi Wang, Zixiang Xu, Zeyu Zhang, Xiaoqing Zhang, Qian Jiang, Zhenhao Chen, et al. Maniplvmr1: Reinforcement learning for reasoning in embodied manipulation with large vision-language models. *arXiv preprint arXiv:2505.16517*, 2025.

[49] Xilong Sun, Jiqing Li, Anna Vladimirovna Kovalenko, Wei Feng, and Yongsheng Ou. Integrating reinforcement learning and learning from demonstrations to learn non-prehensile manipulation. *IEEE Transactions on Automation Science and Engineering*, 20(3):1735–1744, 2022.

[50] Yingbo Tang, Lingfeng Zhang, Shuyi Zhang, Yinuo Zhao, and Xiaoshuai Hao. Roboafford: A dataset and benchmark for enhancing object and spatial affordance learning in robot manipulation. In *Proceedings of the 33rd ACM International Conference on Multimedia*, pages 12706–12713, 2025.

[51] Generalist AI Team et al. Gen-0: Embodied foundation models that scale with physical interaction. *generalist ai blog*, 2025.

[52] Edmond Tong, Anthony Oripipi, Stanley Lewis, Zhen Zeng, and Odest Chadwicke Jenkins. Oval-prompt: Open-vocabulary affordance localization for robot manipulation through llm affordance-grounding. *arXiv preprint arXiv:2404.11000*, 2024.

[53] Tarik Tosun, Eric Mitchell, Ben Eisner, Jinwook Huh, Bhoram Lee, Daewon Lee, Volkan Isler, H Sebastian Seung, and Daniel Lee. Pixels to plans: Learning non-prehensile manipulation by imitating a planner. In *2019 IEEE/RSJ International Conference on Intelligent Robots and Systems (IROS)*, pages 7431–7438. IEEE, 2019.

[54] Dexin Wang, Chunsheng Liu, Faliang Chang, and Yichen Xu. Hierarchical diffusion policy: manipulation trajectory generation via contact guidance. *IEEE Transactions on Robotics*, 2025.

[55] Maozhen Wang, Aykut Özgün Önol, Philip Long, and Taşkin Padir. Contact-implicit planning and control for non-prehensile manipulation using state-triggered constraints. In *The International Symposium of Robotics Research*, pages 189–204. Springer, 2022.

[56] Bowen Wen, Wei Yang, Jan Kautz, and Stan Birchfield. Foundationpose: Unified 6d pose estimation and tracking of novel objects. In *Proceedings of the IEEE/CVF Conference on Computer Vision and Pattern Recognition*, pages 17868–17879, 2024.

[57] Ruinian Xu, Fu-Jen Chu, Chao Tang, Weiyu Liu, and Patricio A Vela. An affordance keypoint detection network for robot manipulation. *IEEE Robotics and Automation Letters*, 6(2):2870–2877, 2021.

[58] Wenhao Yan and Jie Chu. FoundationPose++, March 2025. URL <https://github.com/teal024/FoundationPose-plus-plus>.

[59] Wen Yang, Zhixian Xie, Xuechao Zhang, Heni Ben Amor, Shan Lin, and Wanxin Jin. Twintrack: Bridging vision and contact physics for real-time tracking of unknown dynamic objects. *arXiv preprint arXiv:2505.22882*, 2025.

[60] William Yang and Michael Posa. Dynamic on-palm manipulation via controlled sliding. 2024.

[61] Yuxiang Yang, Tingnan Zhang, Erwin Coumans, Jie Tan, and Byron Boots. Fast and efficient locomotion via learned gait transitions. In *Conference on robot learning*, pages 773–783. PMLR, 2022.

[62] Xili Yi and Nima Fazeli. Precise object sliding with top contact via asymmetric dual limit surfaces. *arXiv preprint arXiv:2305.14289*, 2023.

[63] Zhao-Heng Yin, Binghao Huang, Yuzhe Qin, Qifeng Chen, and Xiaolong Wang. Rotating without seeing: Towards in-hand dexterity through touch. *arXiv preprint arXiv:2303.10880*, 2023.

[64] Zhitong Zhang, Xu Chang, Hongxu Ma, Honglei An, and Lin Lang. Model predictive control of quadruped robot based on reinforcement learning. *Applied Sciences*, 13(1):154, 2022.

[65] Tony Z Zhao, Vikash Kumar, Sergey Levine, and Chelsea Finn. Learning fine-grained bimanual manipulation with low-cost hardware. *arXiv preprint arXiv:2304.13705*, 2023.

[66] Wenzuan Zhou, Bowen Jiang, Fan Yang, Chris Paxton, and David Held. Hacman: Learning hybrid actor-critic maps for 6d non-prehensile manipulation. *arXiv preprint arXiv:2305.03942*, 2023.

[67] Yifeng Zhu, Abhishek Joshi, Peter Stone, and Yuke Zhu. Viola: Imitation learning for vision-based manipulation with object proposal priors. In *Conference on Robot Learning*, pages 1199–1210. PMLR, 2023.

[68] Zixuan Zhuang, Le Zheng, Wanyue Li, Renming Liu, Peng Lu, and Hui Cheng. Rm-planner: Integrating reinforcement learning with whole-body model predictive control for mobile manipulation. In *2025 IEEE International Conference on Robotics and Automation (ICRA)*, pages 7263–7269. IEEE, 2025.

## APPENDIX

### A. Detailed Task Setting in Sim and Real

1) *Robot Operational Space Control*: In the simulated experiments with full robot system, a Operational Space Controller (OSC) is implemented to transform the desired end-effector Cartesian space displacement output of Comfree-MPC to torque command in joint space. In the real-world testing with Franka robot arm, the robot is controlled by an OSC implemented in the panda-py library [13]. The controller executes at 500 Hz, enabling fast reaction to the end-effector displacement command during manipulation.

2) *Robot Motion Planning for Contact Locations*: Between contacts, the end-effector is lifted to disengage from the object and repositioned using OSC in free space. The OSC then guides the end-effector to the next intended contact location, where control switches back to the MPC for contact-rich interaction.

3) *Distribution of Initial and Target Pose*: For each task, the initial and target translation of  $xy$  coordinates are shown in Table IV. Note that we use (P) to stand for Geometry-generalized pushing and (R) to stand for 3D object reorientation, and use Abstract, Full-Sim, Full-Real to stand for abstract end-effector setting, full robot setting in simulation, and real-robot setting. Additionally, each pushing target orientation is a planar rotation with an random  $[-180^\circ, 180^\circ]$  angle about the  $z$ -axis, and each flipping target is defined a fixed  $180^\circ$  rotation about the  $x$ -axis, and an additional rotation with a random  $[-180^\circ, 180^\circ]$  angle about the  $z$ -axis.

TABLE IV: Initialization and target distributions for all tasks.

Task	Init Translation ( $x \times y$ )	Target Translation
Abstract (P)	$[-0.25, 0.25]^2$	Same as init
Full-Sim (P)	$[0.4, 0.6] \times [-0.1, 0.1]$	Same as init
Full-Real (P)	$[0.4, 0.6] \times [-0.3, 0.3]$	$[0.4, 0.5] \times [-0.1, 0.1]$
Abstract (R)	$[-0.1, 0.1]^2$	Same as init
Full-Sim (R)	$[0.4, 0.6] \times [-0.1, 0.1]$	Same as init
Full-Real (R)	$[0.45, 0.5] \times [-0.05, 0.05]$	Same as init

Success thresholds of all tasks are shown in Table V. The translational and orientational distance are shown in (9). The rotation distance is defined as  $1 - \langle \mathbf{r}_H^{\text{obj}}, \bar{\mathbf{r}}^{\text{target}} \rangle^2$ . A trial is considered successful if the object satisfies both thresholds.

TABLE V: Success Threshold for all tasks.

Task	Trans Threshold (m)	Rot Threshold
Abstract (P)	0.05	0.05
Full-Sim (P)	0.03	0.05
Full-Real (P)	0.03	0.02
Abstract (R)	0.08	0.05
Full-Sim (R)	0.05	0.05
Full-Real (R)	0.075	0.03

### B. Settings of RL policy, reward and training

#### 1) RL Policy Setting:

a) *Pointnet++ Setting in RL policy*: We employ two PointNet++ feature extractors—a *Geometric Processing Branch* for dense per-point reasoning and a *Global Kinematic Processing Branch* for object-level aggregation. The Geometric Processing Branch follows a segmentation-style PointNet++ architecture, the Global Kinematic Processing Branch follows a classification-style PointNet++ architecture. Those two branches shares the same Pointnet++ setting, as shown in Table VI. We use the implementation of Pointnet++ networks in pytorch-geometric library [14]. Specifically, although the nominal input channel number is 4 (per-point goal flow and contact-distance features), the 3D keypoint coordinates themselves are normalized and concatenated to this input inside the module.

TABLE VI: PointNet++ hyperparameters.

Parameter	Value
Input channels	4
Output feature dimension	128
Dropout	0.0
Farthest point sampling random start	True
Include point coordinates in Input	True
Position normalization	True
Activation	LeakyReLU

b) *MPC weights action space*: We choose  $\mathcal{W}_{\text{pos}} = \{0, 50, 100, 150, 200\}$  and  $\mathcal{W}_{\text{ori}} = \{0, 2, 4, 6, 8\}$ .

2) *Scaling of Observation*: To improve training stability and generalization across objects of different sizes, all observation components are normalized (divided) by the characteristic size of the object. We set this size to be 0.15 for all letters, and 0.10 for the cube.

3) *RL Reward Setting*: The reward hyperparameter is set to be  $w_1 = 0.1, w_2 = 5.0$  for both tasks, and  $w_3 = 0$  for Geometry-generalized pushing,  $w_3 = 1$  for 3D object reorientation. Specifically, to calculate the term  $\frac{1}{N} \sum_{\delta_{i,k} \in \Delta \mathcal{P}_k} \|\delta_{i,k}\|$ , we use the target component after scaling.

4) *RL Training Setting*: All reinforcement-learning experiments use Proximal Policy Optimization (PPO) in Stable-Baselines3 [43] with the hyperparameters summarized in Table VII. The only exception is  $n_{\text{steps}}$  in end-to-end model baseline comparison, which is set to be 128 to match its higher decision frequency. All hyperparameters are carefully tuned to ensure stable optimization and strong empirical performance across both pushing and flipping tasks. The proposed policy outputs a structured action  $\mathbf{a}_k$  composed of multiple discrete components, corresponding to different aspects of contact intention and MPC parameterization. During training, the log-probability and entropy terms used in the PPO objective are computed as sums over individual components, enabling balanced policy update. During training, two tricks of temperature scaling and learning rate scheduling are used:

a) *Tempertaure Scaling of Logits*: During training, a temperature scaling of 0.1 (i.e., scaling the logits by a factor of 10) is applied to the contact-selection logits to sharpen the resulting categorical distribution and improve learning efficiency, while the logits corresponding to the MPC cost

TABLE VII: PPO hyperparameters used across all experiments.

Parameter	Value
Number of environments ( $n_{\text{envs}}$ )	32
Rollout length ( $n_{\text{steps}}$ )	32
Optimization epochs ( $n_{\text{epochs}}$ )	5
Batch size	512
Clipping range ( $\epsilon$ )	0.3
Discount factor ( $\gamma$ )	0.99
GAE parameter ( $\lambda$ )	0.95
Entropy coefficient ( $c_{\text{ent}}$ )	0.0
Value loss coefficient ( $c_{\text{vf}}$ )	0.5

weights are used without additional scaling. After the scaling process, a softmax function is applied on logits to form the discrete probability distribution among contact point/ MPC weights selection during training.

*b) Learning-Rate Scheduling.*: We employ a monotonically decaying learning-rate schedule of the form

$$\text{LR}(p) = 10^{-4} \cdot \beta^{(p-1)}, \quad p \in [1, 0],$$

where  $p$  denotes normalized remaining training progress from start ( $p=1$ ) to end ( $p=0$ ). For the main experiments, we set  $\beta = 100$ . In the baseline comparisons, we use a smaller decay factor  $\beta = 10$  on end-to-end and HACMan style models to enable stronger updates. In ablation studies, we still set  $\beta = 100$ .

### C. MPC Setting in Sim and Real

While the core MPC formulation is shared across all experiments, physical parameters are adjusted differently for sim/real task to reflect their distinct physical properties. Table VIII summarizes these task-dependent settings. Among those parameters,  $M$  in (7) is formed by:

$$M = \mathbf{diag}(m, m, m, \mathbf{i}, \mathbf{i}, \mathbf{i}, h^2 K_r, h^2 K_r, h^2 K_r) \quad (10)$$

to match the 9 DOFs of the system with the abstract end-effector (6 for object, 3 for robot). In the equation above,  $m$  stands for object mass,  $\mathbf{i}$  stands for the rotation inertia,  $K_r$  is the stiffness of the robot end-effector. Note that these parameters do not necessarily correspond to the true physical values of the object or the robot in the environment. Rather than aiming for exact physical fidelity, these parameters are tuned to provide a stable and effective predictive model for real-time planning.  $K, h$  along with  $M$  are then used in (7).  $H, w_c$  and the control range scale is used to parameterize the optimization problem (2).  $\mu$  is used in the calculation of the Jacobian of the dual cones  $\tilde{J}$  in (7). In simulated abstract and full robot system test, all experiments shares the same MPC parameter. In real-world Geometry-generalized pushing (Real-P) and real-world 3D object reorientation (Real-R), MPC parameter is adjusted to fit the physical properties of the system. Importantly, these adjustments are lightweight, physically intuitive, and do *not* require retraining the RL policy, as the policy reasons only on contact intention. For details of how to form the dynamics (7) and MPC optimization problems (2) using those parameters, please refer to [25].

TABLE VIII: Task-specific MPC parameter settings.

Param	Simulation	Real-P	Real-R
Dynamics time step $h$	0.01	0.01	0.01
Robot stiffness $K_r$	0.01	0.01	0.01
MPC horizon $H$	3	3	3
Contact weight $w_c$	0.2	0.05	0.2
Object inertia $\mathbf{i}$	0.0005	0.0001	0.001
Object mass $m$	0.2	0.05	0.2
Control range scale	0.03	0.015	0.02
Stiffness coefficient $K$	5.0	5.0	0.75
Friction coefficient $\mu$	0.5	0.5	1.0
Environment Steps $T$	20	20	20

### D. Detailed Settings in End-to-End Comparison

*1) Task and Action Space*: For simplicity, this comparison is conducted for the T-pushing task. The task setting is the same as the geometry-generalized pushing task, while the only object used in training and evaluation is "T". For the action space, the end effector is constrained to move in the  $xy$ -plane with a fixed  $z$  position, with a range  $[-0.05, 0.05]^2$  representing delta  $xy$  motions.

*2) Random Perturbations for Robustness Evaluation*: Three types of random perturbation is performed:

*a) External Force*: random forces and torques of  $\mathcal{N}(0, 0.03)$  is applied on all axis of the object at each simulation step.

*b) Friction*: the friction parameter of the object is randomized by a random multiplier, with uniform distribution on  $[0.1, 3.0]$  at each simulation step.

*c) Actuation*: Actuator proportional parameter (100 in training environment) is randomized uniformly between  $[50, 150]$  at each simulation step. Actuator differential parameter (0 in training environment) is randomized uniformly between  $[0, 15]$  at each simulation step.